Check for updates

Machine learning assisted fast prediction of inertial lift in microchannels†

Jinghong Su, [iD] ‡[abc] Xiaodong Chen, [iD] ‡[d]
Yongzheng Zhu [iD] [bc] and Guoqing Hu [iD] *[a]

Inertial effect has been extensively used in manipulating both engineered particles and biocolloids in microfluidic platforms. The design of inertial microfluidic devices largely relies on precise prediction of particle migration that is determined by the inertial lift acting on the particle. In spite of being the only means to accurately obtain the lift forces, direct numerical simulation (DNS) often consumes high computational cost and even becomes impractical when applied to microchannels with complex geometries. Herein, we proposed a fast numerical algorithm in conjunction with machine learning techniques for the analysis and design of inertial microfluidic devices. A database of inertial lift forces was first generated by conducting DNS over a wide range of operating parameters in straight microchannels with three types of cross-sectional shapes, including rectangular, triangular and semicircular shapes. A machine learning assisted model was then developed to gain the inertial lift distribution, by simply specifying the cross-sectional shape, Reynolds number and particle blockage ratio. The resultant inertial lift was integrated into the Lagrangian tracking method to quickly predict the particle trajectories in two types of microchannels in practical devices and yield good agreement with experimental observations. Our database and the associated codes allow researchers to expedite the development of the inertial microfluidic devices for particle manipulation.

I. Introduction

Inertial migration was first observed in a circular tube in which the particles converge into a ring having a radius approximately 0.6 times the tube radius.[1] However, inertial effects have long been ignored in microfluidic applications because the fluids within microchannels often flow at very low Reynolds numbers.[2] In 2007, Di Carlo *et al.* published a paper showing how to use inertia to focus and separate particles in microchannels.[3] This paper sparked the enthusiasm of the scientific community and soon many new works demonstrated that inertial effects are capable of achieving the high-throughput manipulation of diverse particles in microfluidic platforms.[4–11] The migration of

particles profoundly depends on many variables including particle size, channel geometry, and flow conditions.[12–18] To develop inertial microfluidic devices with optimal performance for particle manipulation, it is necessary to predict the equilibrium positions of targeted particles under different operating conditions, mainly by estimating the inertial lift forces on particles in confined flows.

Both theoretical analyses and numerical simulations have been used to calculate inertial lift forces on small particles. Most theoretical studies were conducted by solving the Navier–Stokes equations using the perturbation methods. Ho and Leal proposed an explicit inertial lift formula that can explain the inertial focusing patterns in planar or tube Poiseuille flows.[12] Vasseur and Cox also deduced an inertial lift formula from the solution of the next-order equations that accounts for a non-linear coupling between the disturbance and the stokeslet disturbance.[19] However, the requirement of small Reynolds number (Re = $\rho U_{\max} H / \eta$, where ρ is the fluid density, $U_{\max}$ the maximum channel velocity, H the channel height, η the dynamic viscosity) in deducing lift formula makes their method inapplicable if the Reynolds number further increases. Using the matched asymptotic perturbation method, Schonberg & Hinch[20] and Asmolov[21] extended the applicable Reynolds number up to 150 and 3000, respectively. Still, it is difficult to directly use

[a] *Department of Engineering Mechanics, State Key Laboratory of Fluid Power and Mechatronic Systems, Zhejiang University, Hangzhou 310027, China.*
E-mail: ghu@zju.edu.cn
[b] *The State Key Laboratory of Nonlinear Mechanics (LNM), Institute of Mechanics, Chinese Academy of Sciences, Beijing 100190, China*
[c] *School of Engineering Science, University of Chinese Academy of Sciences, Beijing 100049, China*
[d] *School of Aerospace Engineering, Beijing Institute of Technology, Beijing 100081, China*
† Electronic supplementary information (ESI) available. See DOI: 10.1039/d1lc00225b
‡ Equal contribution.

these theoretical results to predict the inertial lift of finite-sized particles in three-dimensional rectangular channels, which is the common situation in inertial microfluidic applications.[14,22–24]

The challenge inherent to solving for the inertial lift in more complicated geometries led to the use of direct numerical simulation (DNS) because DNS can provide crucial information that is otherwise unavailable from experiments and theories.[24–26] Using the lattice Boltzmann method, Chun et al. found eight equilibrium positions in square channels at Re = 100.[27] Di Carlo et al. developed a DNS method to obtain the inertial lift acting on a particle by fixing the particle at specific positions of the channel cross-section.[28] Using the arbitrary Lagrangian–Eulerian method (ALE), Yang et al. investigated the inertial lift on a sphere in a tube and proposed an inertial lift formula similar to the classical one of aerodynamics.[29] Asmolov et al. numerically studied the inertial focusing of finite-sized particles in straight microchannels and generalized expressions of the inertial lift to finite-sized particles in a channel flow at Re ≤ 20.[9] In spite of being the only means to accurately obtain the lift forces, DNS often consumes high computational cost and even becomes impractical when applied to complex geometries encountered in real-world microfluidic devices, for example, long serpentine or spiral channels.[24,30–36] By correcting Ho and Leal's formula,[12] we recently proposed a generalized explicit inertial lift formula based on the DNS data obtained in straight microchannels.[37]

Incorporated properly into the Lagrangian tracking scheme, this generalized formula can greatly reduce the computational cost to predict the particle trajectories in complex microchannels for inertial microfluidic applications.[37,38] However, the formula is too complex to be used with ease by the researchers who do not have much knowledge in computational fluid dynamics. Moreover, the implementation of this formula for different problems requires a look-up table generated from the computationally-heavy DNS.[39]

In this work, we developed a fast numerical algorithm in conjunction with machine learning techniques for the prediction of inertial lifts in microchannels. A database of inertial lift forces was constructed by conducting DNS over a wide range of operating parameters in straight microchannels with three types of cross-sectional shapes, including rectangular, triangular and semicircular shapes. The machine learning assisted model was then used to obtain the inertial lift distribution in the channel cross-section, by simply specifying the channel shape, Reynolds number, particle blockage ratio. The resultant inertial lift was integrated into the Lagrangian tracking scheme to quickly predict the particle trajectories in two types of microchannels, yielding good agreements with the corresponding experimental observations. Our database and associated codes allow researchers to expedite the development of the inertial microfluidic devices for particle manipulation.
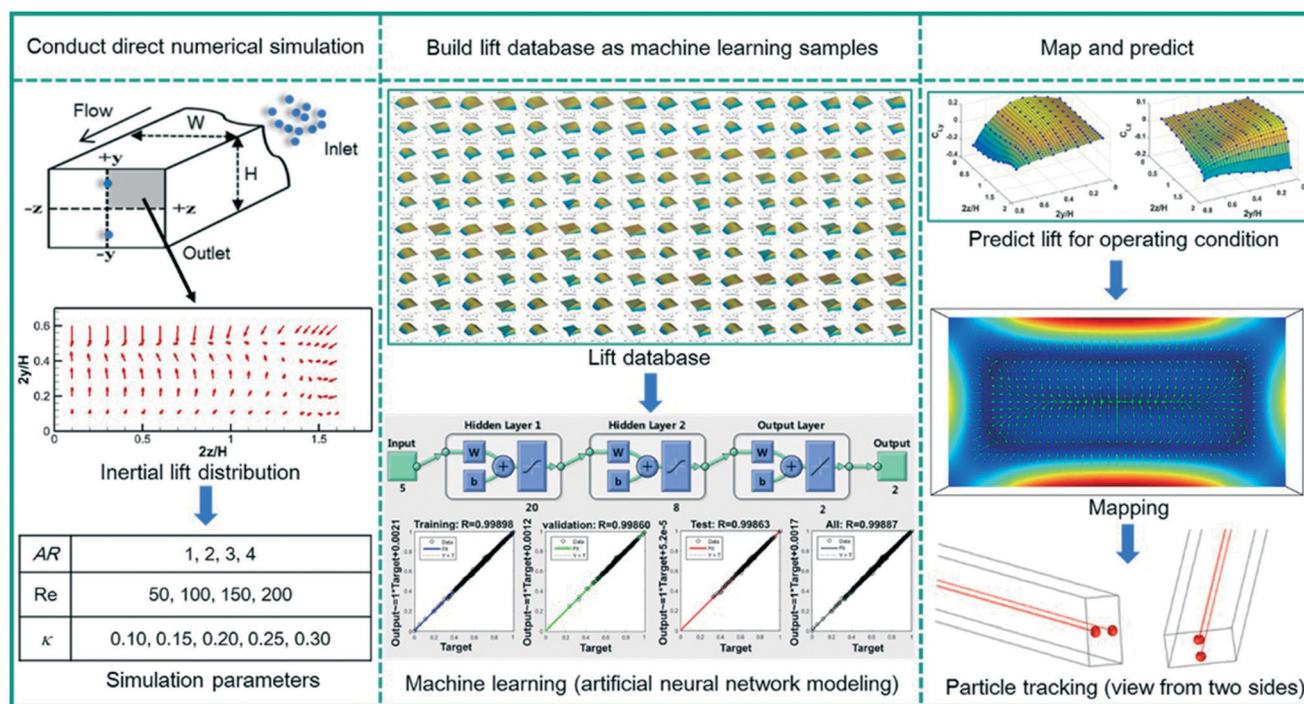

Fig. 1 An overview of the prediction process in three steps illustrated in three columns. The first step: distributions of inertial lift forces on spherical particles in cross-sections of rectangular microchannels were calculated in a wide parameter space as shown in the table using direct numerical simulations; the second step: based on the simulation results, a force database was built (the enlarged pictures of the database and the data file are given in the ESI†) and used as machine learning samples to establish a prediction model; the third step: using the prediction model, the distribution of inertial lift forces was obtained and mapped to the cross-section to predict the particle trajectories.

II. Methods

Fig. 1 shows an overview of machine learning assisted fast prediction of inertial lift forces experienced by spherical particles in microchannels. Taking the rectangular channel as an example, the process was carried out in the following three steps: (I) conduct direct numerical simulations – distributions of inertial lift forces on cross-sections of microchannels were calculated in a wide parameter space; (II) build lift force database as machine learning samples – machine learning was performed upon the database of the inertial lift to model variations of the distributions with controlling parameters; (III) map and predict – the distribution of inertial lift for a given set of parameters was obtained from the model and mapped to the channel cross-section for predicting the particle trajectories.

A. Calculation of inertial lift

Taking a straight microchannel with rectangular cross-section for example, spherical particles located at different lateral positions ($2y/H$, $2z/H$) will experience different inertial lift forces. The inertial lift, F_L, on neutrally buoyant spherical particles in a straight microchannel is generally determined by a total of seven geometric and physical parameters.[14] The formula of F_L can be written as

$$F_L = F(H, a, U_{max}, \eta, \rho, y, z), \qquad (1)$$

where (y, z) is the coordinate in the y–z plane as shown in the channel schematic in Fig. 1. Among these parameters, H, U_{max} and ρ were used to nondimensionalize the system. According to the Buckingham π theorem,[40]

$$F_L = F\left(1, \frac{a}{H}, 1, \frac{\eta}{\rho U_{max} H}, 1, \frac{2y}{H}, \frac{2z}{H}\right) = F\left(\kappa, Re, \frac{2y}{H}, \frac{2z}{H}\right), \quad (2)$$

where $\kappa = a/H$ is the particle blockage ratio. The dimensionless parameters, κ and Re, represent particle size and flow condition, respectively. The lateral position of the center of the spherical particle is ($2y/H$, $2z/H$).

Three-dimensional direct numerical simulations were conducted to calculate F_L by using the Overture object-oriented framework.[41] Herein, the Navier–Stokes (N–S) equations for incompressible flow and Newton's second law for particle motion were numerically coupled. The N–S equations are

$$\nabla \cdot \boldsymbol{u} = 0, \qquad (3)$$

$$\frac{\partial \boldsymbol{u}}{\partial t} + (\boldsymbol{u} \cdot \nabla)\boldsymbol{u} = -\frac{1}{\rho}\nabla p + \frac{\eta}{\rho}\nabla^2 \boldsymbol{u}, \qquad (4)$$

where $\boldsymbol{u}$ is the fluid velocity tensor, t is the time, and p is the pressure. The equations for particle motions are

$$m_p \frac{d\boldsymbol{U}_p}{dt} = \int_{\sum} (-p\mathbf{1} + \boldsymbol{\tau}) \cdot \boldsymbol{n} d\sigma, \qquad (5)$$

$$\frac{d[\boldsymbol{I} \cdot \boldsymbol{\omega}_p]}{dt} = \int_{\sum} (\boldsymbol{x} - \boldsymbol{x}_c) \times [(-p\mathbf{1} + \boldsymbol{\tau}) \cdot \boldsymbol{n}] d\sigma, \qquad (6)$$

where $\boldsymbol{\omega}_p = [\omega_1 \ \omega_2 \ \omega_3]^T$ is the angular velocity vector, $\mathbf{1}$ is the unit tensor, $\boldsymbol{\tau}$ is the shear rate tensor, $\boldsymbol{n}$ is the unit normal vector of the particle surface, $\boldsymbol{I} = \text{diag}(8\pi\rho a^5/15)$ is the moment of inertia tensor of the particle, and $\boldsymbol{x}_c$ is the position of the particle centroid.

The no-slip boundary condition was imposed on the channel walls and particle surface. A fully developed Poiseuille flow velocity profile for the channel cross-section was imposed at the inlet. The constraint of $p + \partial p/\partial n = 0$ was imposed at the outlet. The entire grid was constructed based on the overlapping grid method.[42] Information exchanges of the subzones were achieved via interpolation between every two overlapping grid blocks. These overlapping grid blocks were continuously updated during the iteration process to ensure quality. The solving process was done by PETSc software package,[42] a dynamic link library of the Overture framework.

To calculate the inertial lift at a predefined lateral position, the lateral velocity (U_y and U_z) was set to be zero. Particles were limited to translate only in the axial direction of the channel but could rotate freely. Once the translational and rotational motions both reached steady states, the inertial lift at different lateral positions was obtained. F_L is composed of two components in y and z direction, F_{Ly} and F_{Lz}, respectively. The inertial lift coefficient C_L was used to normalize the inertial lift acting on spherical particles[12] as

$$C_L = \frac{F_L}{(\rho U_{max}^2 a^4/H^2)}. \qquad (7)$$

C_{Ly} and C_{Lz} are the two components of C_L in y- and z-direction, respectively. More details about the simulation process and the calculation of the inertial lift can be found in our previous works.[13,14,36] Similar process was conducted to calculate the inertial lift for the straight microchannels with triangular and semicircular cross-section shapes.

B. Machine learning algorithms

Artificial neural network (ANN) modeling is a powerful supervised machine learning algorithm that can train complex fitting and classification problems. Most of the normal fitting schemes require prior knowledge of the functional relationship between the independent variables and the dependent variables in order to perform purposeful fitting and extrapolation. By contrast, machine learning does not require prior knowledge of functional relationships. With enough data, the neural network can learn and capture the subtle functional relationships, even if the underlying relationships are unknown or difficult to describe. Considering the complicated fluid mechanics involved in the particle migration and thus many parameters affecting the inertial lift forces, it would be advantageous to apply the neural network method to build the prediction model. The

neural network consists of many connected basic elements (neurons), which can mimic the behavioral characteristics of animal neural networks for the distributed and parallel information processing.[43] The structure and function of each neuron are relatively simple, but the system behavior produced by a large number of neuron combinations can be very complicated. Since the neural network can change the value of synaptic weights to meet the requirement of the surrounding environment during the learning process, it has self-adaptation and self-organization capabilities.[44,45] Recently, the neural network has been widely used in microfluidics.[46,47]

Here, we adopted the most popular error backpropagation neural network (BP neural network).[48] The structure of the BP neural network includes three types of network layers – the input layer, hidden layer, and output layer.[49] As shown in Fig. 2, two hidden layers were used in the present study. All the network layers are made up of neurons. Only neurons in two adjacent layers are connected, while neurons in the same layer are not connected. Each connection corresponds to a weight ($w^n(i,j)$) and a bias ($b^n(j)$), where i corresponds to the neuron i in the layer $n-1$ and j corresponds to the neuron j in the layer n. After being weighted and summed, the output of all the neurons in the layer $n-1$ will be added a bias to obtain the input to the neuron j in the layer n, which is written as $\sum_{i=1}^{sn} w^n(i,j)a^{n-1}(i) + b^n(j)$. The neuron j passes the input through a transfer function $f(x)$ to generate an output,

$$a^n(j) = f\left(\sum_{i=1}^{sn} w^n(i,j)a^{n-1}(i) + b^n(j)\right). \tag{8}$$

where $a^{n-1}(i)$ is the output of the neuron i in the layer $n-1$, and $a^n(j)$ is the output of the neuron j in the layer n.

The BP neural network continuously updates the weights and biases through the forward propagation of the signal and the backpropagation of error to reduce the error to the neural network goal error.[50] The Levenberg–Marquardt optimization algorithm was used here to describe the update formula of the weights or biases ($\boldsymbol{x}$)[51]

$$\boldsymbol{x}_{k+1} = \boldsymbol{x}_k - [\boldsymbol{J}^T\boldsymbol{J} + \mu\boldsymbol{1}]^{-1}\boldsymbol{J}^T\boldsymbol{e}, \tag{9}$$

where $\boldsymbol{J}$ is the Jacobian matrix that contains first derivatives of the errors e_q ($e_q = t_q - o_q$, where t_q is the target value and o_q is the output of the network for the qth input) for the weights or biases, $\boldsymbol{e}$ is the vector of the errors, k is the training step, and μ is the Levenberg's damping factor. The μ is adjusted to reduce the performance index, which is defined as the mean square error, to the training goal error.

To realize the prediction of inertial lift, the model must first have good learning ability, in other words, fitting ability. We found that the effect of polynomial fitting is very poor under large channel aspect ratios, i.e., an overfitting of the inertial lift was found as shown in Fig. 3. We here used the hyperbolic tangent function as the transfer function for neurons in the two hidden layers, i.e.,

$$f(x) = \tanh(x) = \frac{e^x - e^{-x}}{e^x + e^{-x}}. \tag{10}$$

The transfer function of the neuron in the output layer was defined as a linear function by default, i.e.,

$$f(x) = x. \tag{11}$$

The comparison of the performance between polynomial fitting and neural network method for inertial lift was conducted and shown in Fig. 3. The comparison
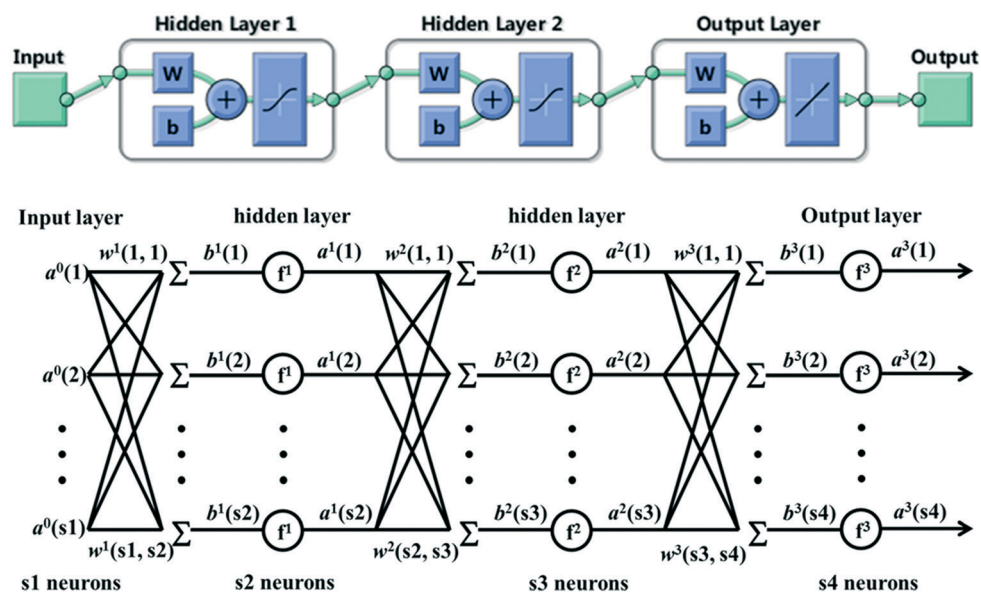

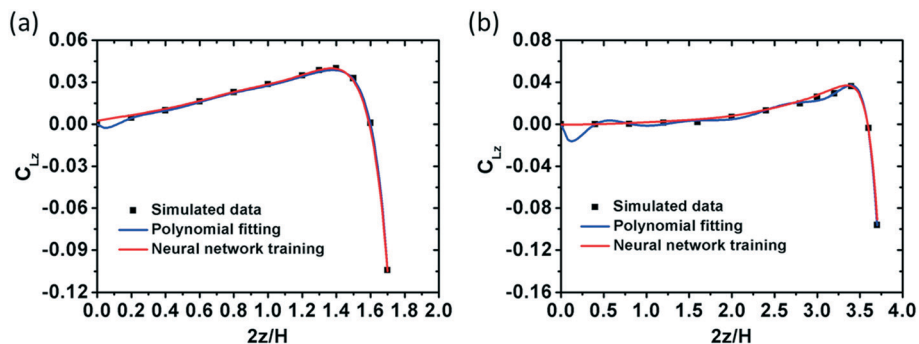Fig. 2 The schematic diagram of the neural network model.

Fig. 3 Comparison of the performance between polynomial fitting and BP neural network method for inertial lift along long axis in rectangular microchannel with Re = 200 and κ = 0.2 at AR = 2 (a) and AR = 4 (b).

demonstrates that the BP neural network method can better capture the functional relationship.

C. Prediction of particle trajectories

After training with the database, the machine learning model was used to predict the distribution of the inertial lift in channel cross-sections for any given conditions within the considered parameter space. The predicted inertial lift was then mapped to the corresponding channel cross-section to track the particle trajectories using a procedure similar to

our previous studies.[52,53] The calculations were performed in COMSOL Multiphysics® modeling software. For a given channel geometry, a no-slip boundary condition was imposed on each channel wall, a constant flow rate at the inlet, and a suppressed backflow boundary condition at the outlet. A steady-state of the flow field without particles was obtained first by solving the incompressible N–S equations. The randomly distributed particles were then released at the inlet, accompanied by imposing a bounce boundary condition on the channel walls and a freezing boundary condition at the outlet. Based on the steady-state solution of the flow field,
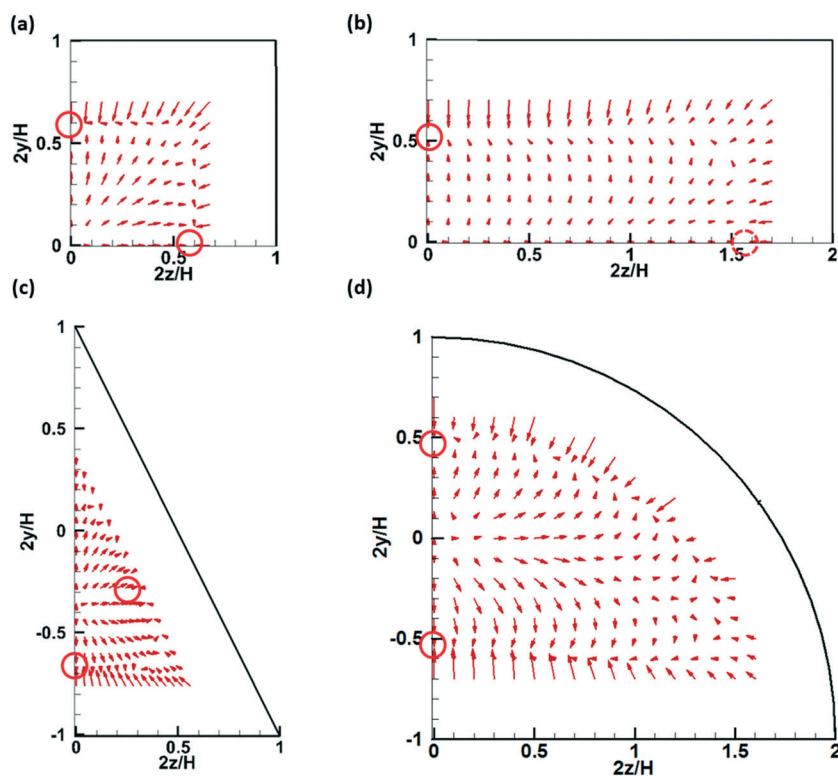

Fig. 4 Distributions of the inertial lift vectors acting on a spherical particle with κ = 0.2 under Re = 100 in channels with different cross-sectional shapes, including a square cross-section (a), a rectangular cross-section (b), a triangular cross-section (c), and a semicircular cross-section (d). Due to symmetry, only a quarter section is shown here for (a) and (b), while a half section is shown for (c) and (d). Each vector represents the inertial lift experienced by a spherical particle with its center at the origin of the vector. The solid-line circles denote the stable equilibrium positions and the dashed-line circles denote the unstable equilibrium positions.

the particle trajectories were calculated by solving Newton's second law of motion:[54]

$$\frac{d\boldsymbol{u}_{\mathrm{p}}}{dt} = \frac{3\mu C_{\mathrm{D}} \mathrm{Re}_{\mathrm{r}}}{4\rho_{\mathrm{p}} a^2}\left(\boldsymbol{u} - \boldsymbol{u}_{\mathrm{p}}\right) + \frac{1}{2}\frac{\rho}{\rho_{\mathrm{P}}}\frac{d\left(\boldsymbol{u} - \boldsymbol{u}_{\mathrm{p}}\right)}{dt} + \frac{6 F_{\mathrm{L}}}{\pi a^3 \rho_{\mathrm{P}}}, \qquad (12)$$

where $\boldsymbol{u}_{\mathbf{p}}$ is the particle velocity, C_{D} is the Stokes drag coefficient, Re_{r} is the relative Reynolds number, and ρ_{P} is the particle density. The first term on the right-hand side of the eqn (12) is the drag force which can drive particles to move along with the fluid flow. The second term is the virtual mass force. The third term is the inertial lift predicted from the method in sec. II.B. Here the inertial lift was explicitly applied to the channel cross-section by a mapping method (see Fig. S2†).

III. Results and discussion

A. Data preparation

Researchers have also explored various cross-sectional microchannels for inertial manipulation of particles.[55] We simulated the inertial lifts for microchannels with three different cross-sectional shapes, including rectangular, triangular, and semicircular (Fig. 4). For each channel, a wide range of parameters were considered, *i.e.*, Re varies from 50 to 200 with an interval of 50, and κ varies from 0.10 to 0.30 with an interval of 0.05. The square channel can be considered as a special case of the rectangular channel with channel aspect ratio AR = 1 (AR = W/H, where W is the channel width). In the parameter space, the square channel always has four stable equilibrium positions near the wall centers.[56] Three types of the rectangular channel with larger AR (2, 3, and 4) were simulated. These rectangular channels have two stable equilibrium positions near the long wall centers and two unstable equilibrium positions near the short wall centers when Re is smaller than a critical value.[14] With the increase of Re, the equilibrium positions near the short wall centers will become stable (Fig. 5). The triangular channel is isosceles with equal base and height. It generates three stable equilibrium positions near the wall centers. For the semicircular channel, there are two stable equilibrium positions at the symmetry axis of the channel. The choice of $2y/H$ and $2z/H$ for the three types of microchannels were given in the ESI.† Intervals of the simulated parameters allow systematical and representative investigation for the rectangular microchannels (totally 8068 cases for 80 operating conditions), triangular microchannels (totally 2420 cases for 20 operating conditions,) and semicircular microchannels (totally 3672 cases for 20 operating conditions).

Considering that the rectangular channel have similar topological structures, we tried to use AR as one of the independent variables for the inertial lift to predict the inertial lift under rectangular cross-section channels with different AR. Fig. 5 shows the typical distributions of the inertial lift on a quarter of the cross-section of the rectangular channels with AR = 2 and 4. Similarities under different AR can be observed, indicating that using AR as an independent variable is feasible. The square channel can be considered as a special case of the rectangular channel with AR = 1. Fig. 6a and b show the distribution of inertial lift by three-dimensional surface for channels with AR = 1, 2, and 4. To obtain better machine learning performance, $2z/H$ was normalized (or scaled) by AR to $(2z/H)/\mathrm{AR}$ ensuring that the inertial lift data are within a consistent geometrical space under different AR. The influences of AR on $C_{\mathrm{L}y}$ and $C_{\mathrm{L}z}$ are shown in Fig. 6c and d, respectively. Variations of the inertial lift along the main axis for AR = 2, 3, and 4 show good similarity. However, variations for AR = 1 show different patterns from the other AR, which was also confirmed by the simulations from other groups.[23,28] Therefore, an additional AR of 1.5 was added (see Fig. S3†) to make the transition more smooth for AR from 1 to 2.
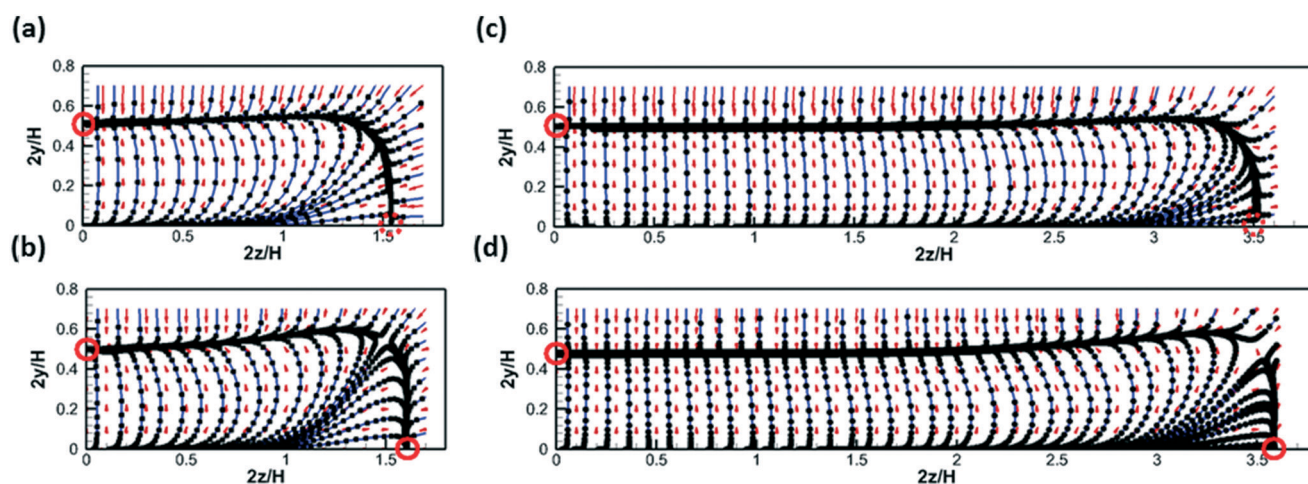

Fig. 5 Distributions of the inertial lift vectors acting on a spherical particle with κ = 0.2 in quarters of cross-sections of rectangular channels with AR = 2 (a and b) and AR = 4 (c and d) under Re = 100 (a and c) and Re = 200 (b and d). Trajectories of the particle center are indicated with the blue lines. Black dots are placed on the trajectories with the same dimensionless time unit.
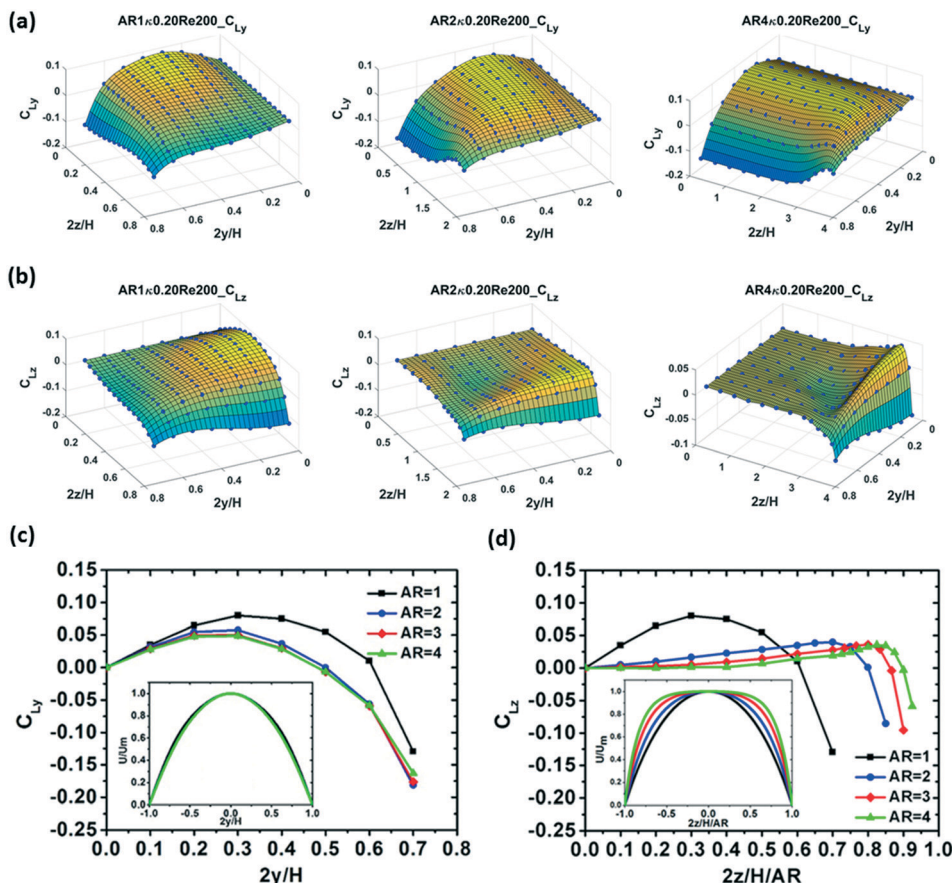
Fig. 6 Distributions of the inertial lift coefficient components in quarter of channel cross-sections with Re = 200 and κ = 0.2. The distributions of C_{Ly} (a) and C_{Lz} (b) are shown by three-dimensional surface for microchannels with AR = 1 (the first column), AR = 2 (the second column) and AR = 4 (the third column). The C_{Ly} along the short axis (c) and C_{Lz} along the long axis (d) are shown at different AR.
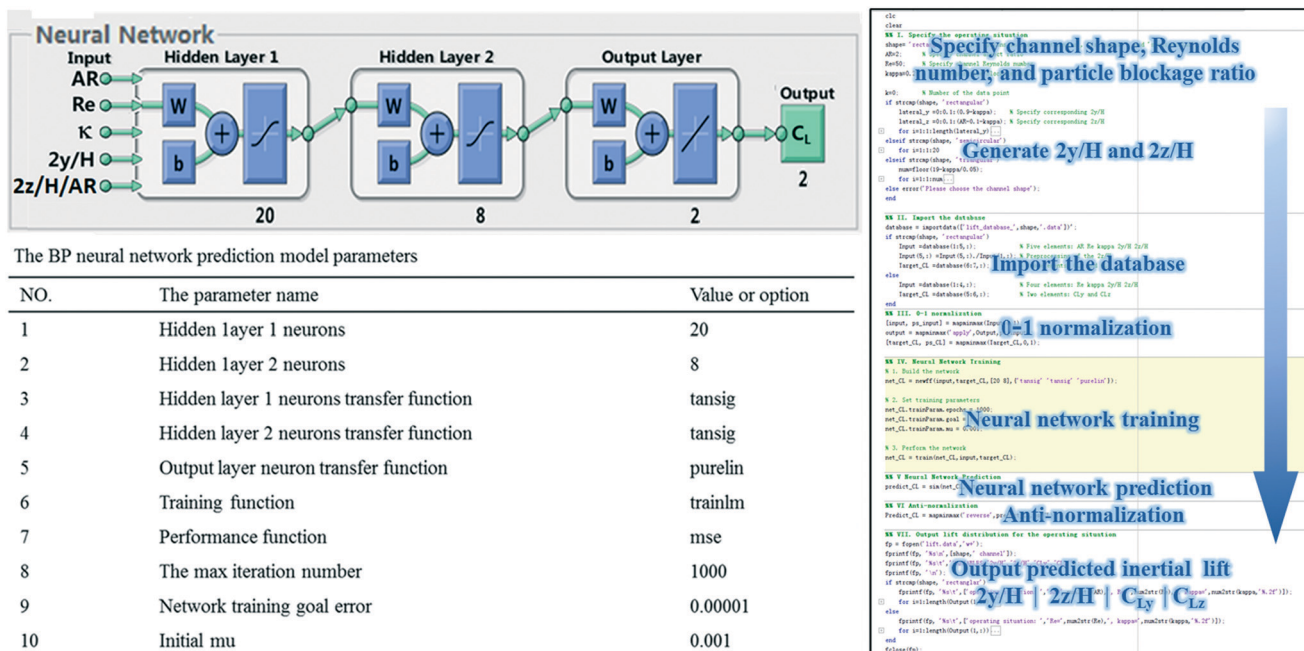

The BP neural network prediction model parameters

NO.	The parameter name	Value or option
1	Hidden layer 1 neurons	20
2	Hidden layer 2 neurons	8
3	Hidden layer 1 neurons transfer function	tansig
4	Hidden layer 2 neurons transfer function	tansig
5	Output layer neuron transfer function	purelin
6	Training function	trainlm
7	Performance function	mse
8	The max iteration number	1000
9	Network training goal error	0.00001
10	Initial mu	0.001

Fig. 7 The neural network prediction model, parameter setting and calculation procedure.

B. ANN model setup

The BP neural network was invoked as the ANN model to train the inertial lift data. Due to the essential difference in topology, it is difficult to extract the AR-like parameter of the triangular channel and the semicircular channel to match the rectangular channel. Therefore, the inertial lift in the triangular channel and the semicircular channel will be independently predicted. The inertial lift in the rectangular channel has 5 independent variables, *i.e.*, AR, Re, κ, $2y/H$, $(2z/H)$/AR. while the inertial lift in the triangular channel and semicircular channel has 4 independent variables, *i.e.*, Re, κ, $2y/H$ and $2z/H$. Here, we took the rectangular channel as an example to introduce the model. As shown in Fig. 7, the

input layer has 5 variables, *i.e.*, AR, Re, κ, $2y/H$ and $(2z/H)$/AR, and the output layer has 2 variables, *i.e.*, C_{Ly} and C_{Lz}. The first and second hidden layers contain 20 and 8 neurons, respectively. The maximum number of iterations is 1000, the training goal error is 0.00001, and the initial Levenberg's damping factor is 0.001. The right column shows the steps to predict the inertial lift distribution for given channel shape, Reynolds number, and particle blockage ratio: (I) once the given situation was input, the corresponding discrete points $[2y/H, 2z/H]$ were automatically generated; (II) the inertial lift database was imported and normalized by the 0–1 normalization method; (III) the neural network training and prediction were conducted with the normalized data; (IV) after anti-normalization, the predicted inertial lift on the
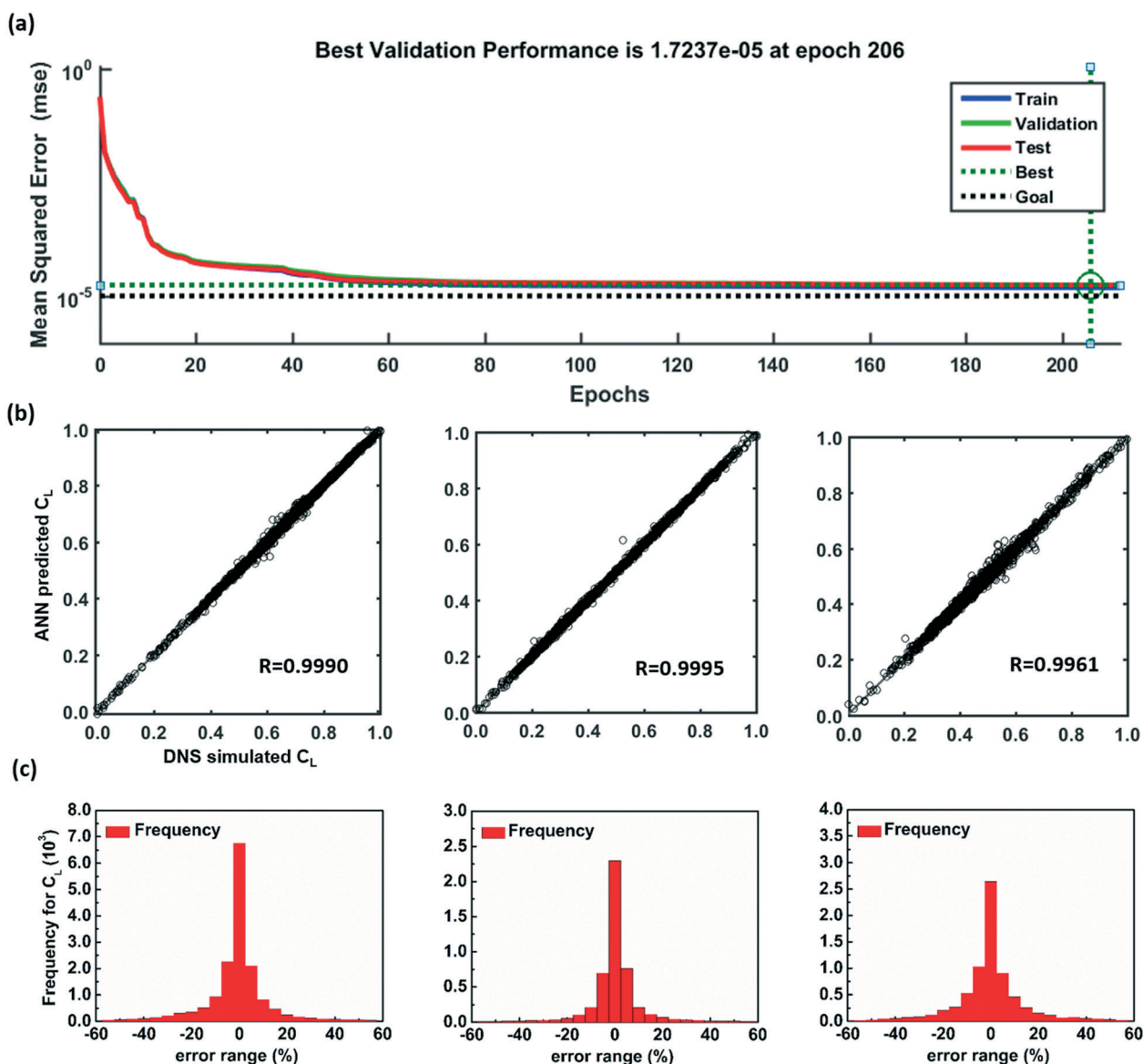

Fig. 8 (a) The performance of the ANN model was verified by measuring the mean square errors of C_L in the rectangular channel during training steps. The predicted data was compared with the simulated data in terms of linear regressions (b) and error distributions (c) for the rectangular channel (first column), triangular channel (second column), and semicircle channel (third column). The data for the linear regressions was normalized by the 0–1 normalization method.

discrete points was output. The process can be executed within several seconds by the MATLAB code as provided in ESI.†

C. Verification and validation

To verify the ANN model, the simulated lift data were randomly divided into three parts: 70% for training (training data), 15% for verification (verification data), and 15% for testing (testing data). The mean squared errors of C_L for the training data, verification data and testing data were measured at each training step. The training data were utilized to adjust the network by updating weights or biases according to eqn (9) and reduce the mean squared error to the training goal error. The verification data were utilized to measure the generalization performance and provided feedbacks to the network. The generalization performance indicates the predictive ability on data outside the training

data and is measured by the mean squared errors of the verification data (green solid line). The adjustment will be halted when the generalization performance stops improving. As shown in Fig. 8a, to ensure a good generalization performance, the adjustment stops when the mean squared error of the verification data is reduced to the training best error (green dotted line) instead of the training goal error (black dotted line). The testing data were used to view the prediction ability of the adjusted network, without contributions to the adjustment. The inertial lift forces were further predicted by the ANN model for all the combinations of the input parameters considered here. The linear regressions were conducted for the predicted results and the simulated results as shown in Fig. 8b, where the correlation coefficients (R) for the inertial lift in the rectangular channel, triangular channel, and semicircular channel is 0.9990, 0.9995, and 0.9961, respectively. All the correlation coefficients are very close to 1, confirming good consistency.
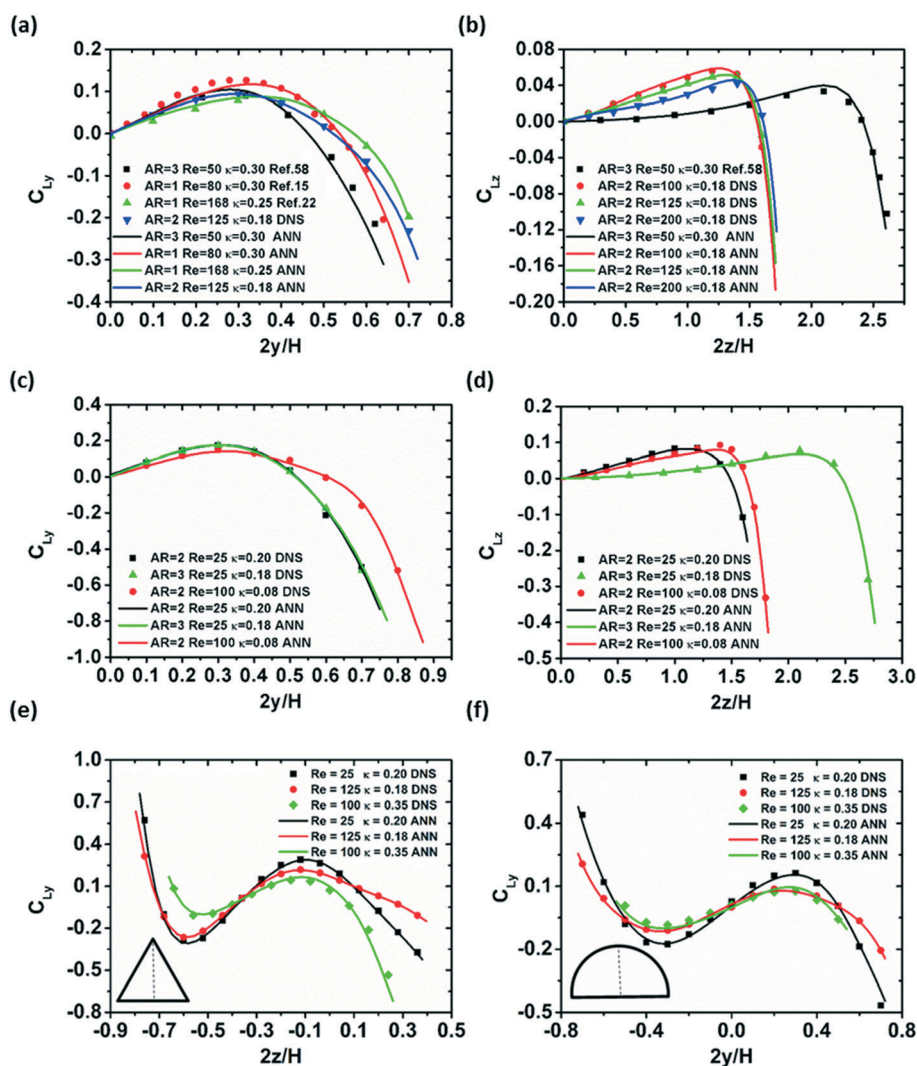

Fig. 9 Comparisons between the inertial lift forces from the direct numerical simulations (symbols) and the ANN predictions (lines). Interpolated predictions (a and b) and extrapolated predictions (c and d) for the inertial lift in the rectangular channel were performed to compare with simulation results. The comparison of the inertial lift in the triangular channel (e) and semicircular channel (f) were also conducted.

Fig. 8c further shows that the most of errors of the predicted data are within 10%.

The adaptability of the ANN model was also verified by predicting the inertial lift under the conditions that were not included in the database. Fig. 9 provides the comprehensive comparisons between the inertial lift from the direct numerical simulations (symbols) and the ANN model (lines) in the rectangular channel (Fig. 9a–d), triangular channel (Fig. 9e) and semicircular channel (Fig. 9f). Fig. 9a and b show C_{Ly} along the centerline in y direction and C_{Lz} along the centerline in z direction, respectively, which were predicted under parameters within the ranges of the database (interpolation). The parameter combinations are (AR, Re, κ) of (1, 80, 0.30),[28] (1, 168, 0.25),[22] (2, 100, 0.18), (2, 125, 0.18), (2, 200, 0.18), and (3, 50, 0.30).[57] On the other hand, Fig. 9c and d display the lift forces under conditions with at least one parameter beyond the rage of the database (extrapolation). Besides, the distributions of C_{Ly} and C_{Lz} on the cross-section of the rectangular channels with AR = 1.5 and 2.5 are given in the Fig. S4.† The interpolated predictions and extrapolated predictions are also performed for triangular channel (Fig. 9e) and semicircular channel (Fig. 9f). All these comparisons show excellent agreement between the DNS and the ANN model, demonstrating the robustness of the present algorithm in the fast prediction of the inertial lift forces in a wide range of operating conditions.

D. Applications in complex microchannels

Knowing particle trajectories prior to fabrication of microfluidic devices is ideal for their design and optimization. To avoid the possible bias from self-comparison, here we chose the experimental results from other groups to compare with our numerical simulations. The particle trajectories in two complex microchannels, a single-position focusing channel with varied cross-sectional shapes,[58] and a multistage rectangular channel,[59] were calculated by the particle tracking method. To capture the particle trajectories from inlet to outlet in such long microchannels by DNS is almost impractical. Here, the inertial lift forces were first obtained for the given channel geometry and flow conditions using the ANN model and the lift database. They were then mapped to the cross-sections of the channels to be explicitly implemented in the last term in eqn (12). Detailed mapping procedures can be found in the ESI.†

The single-position focusing microchannel consists of three parts with different cross-sectional shapes as shown in Fig. 10a. The microchannel changes from a rectangular cross section (2.5 cm long) to a triangular cross section (1 cm long) and then to a semicircular cross section (1 cm long). The geometry in Fig. 10a was displayed at a ratio of 100:1 along the length. The rectangular cross section has a width of 50 μm and AR = 2. The triangular cross section is isosceles with equal base and height. Such arrangement realized the single-position focusing of particles without the need for secondary flow, sheath flow or external forces.[58] Here we simulated the motion of 9 μm particles at inlet average velocity of 1.0 m s^{-1}. Due to the particle focusing in the upstream rectangular cross section, no particle enters the basins of attraction of the bottom focusing position in the triangular and semicircular channels (Fig. 10a and b). The particles successively focus to the two focusing positions in the
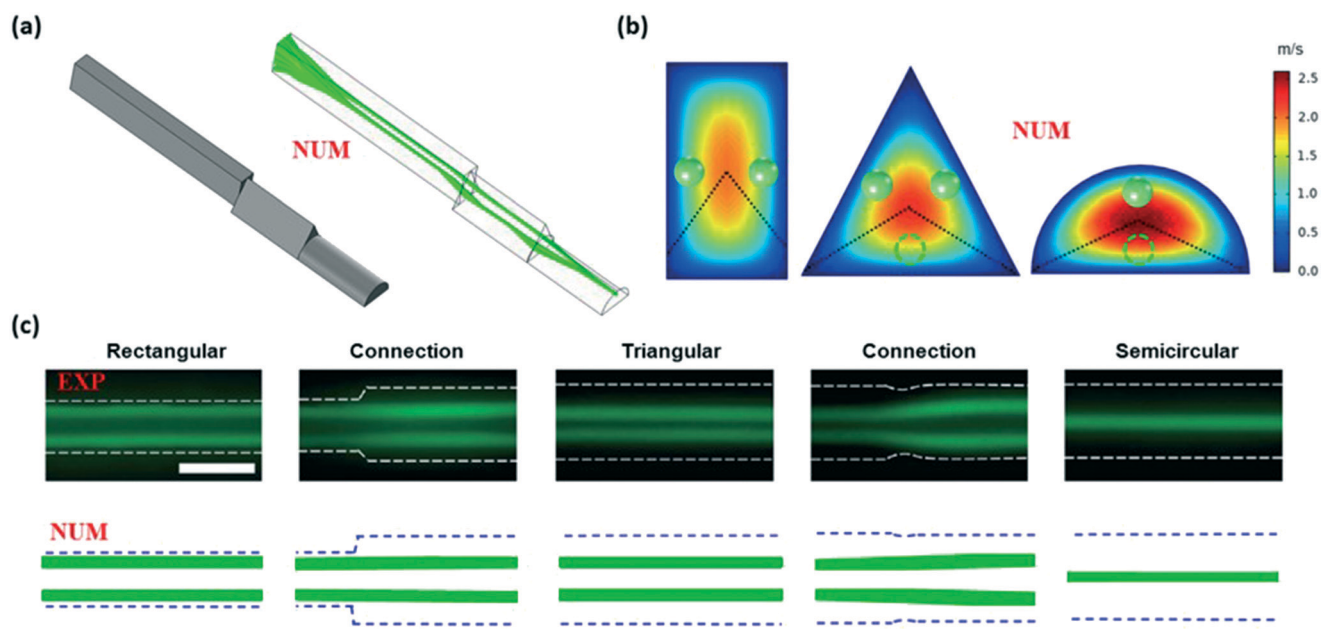

Fig. 10 (a) Schematic diagram of a single-position focusing microchannel with varying cross-sectional shapes and the particle trajectories. (b) Schematic diagram of the focusing patterns of particles in different cross-sectional shapes. (c) Comparison of the particle trajectories between simulations and experiments[58] (experimental images are reproduced from ref. 58 with permission from the Royal Society of Chemistry).
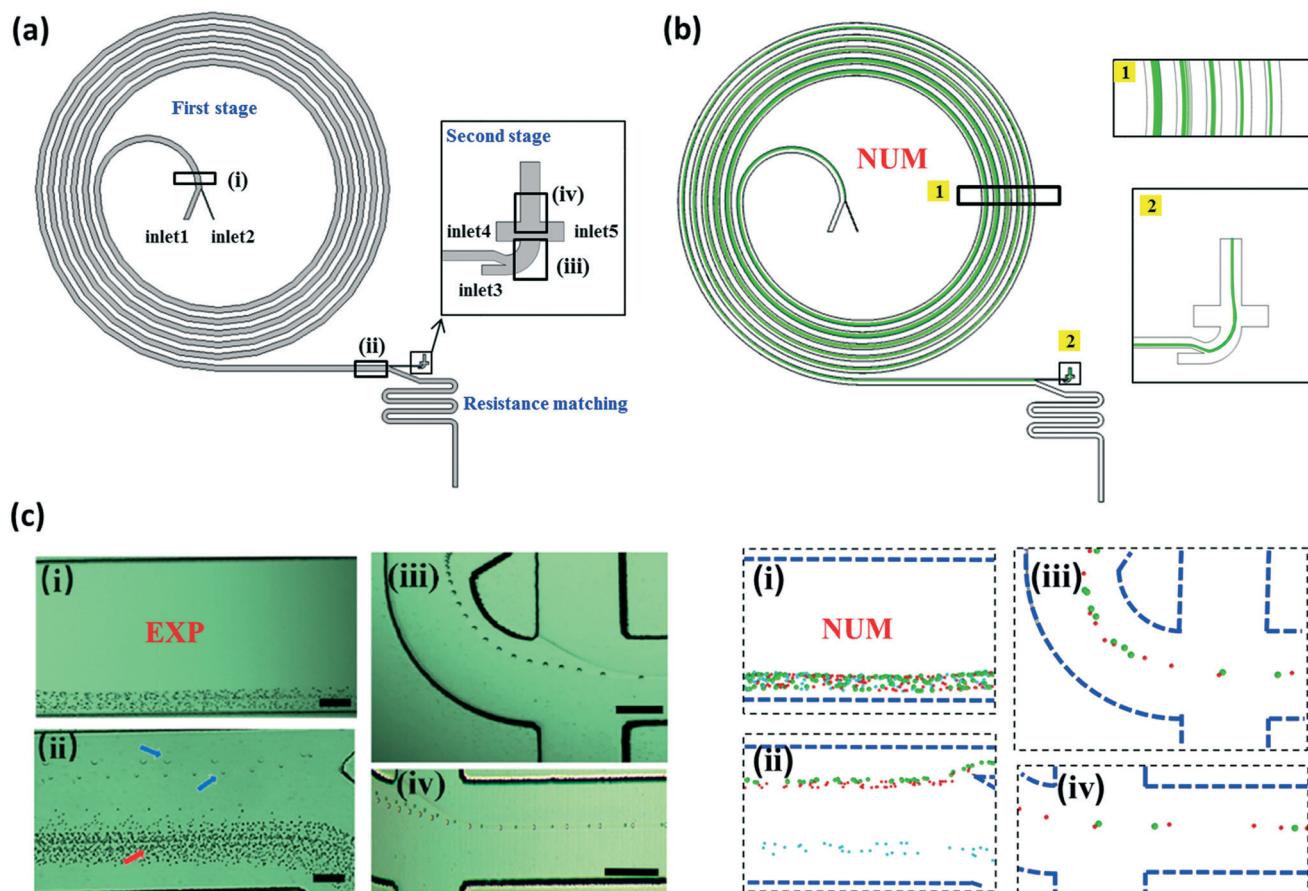
Fig. 11 (a) Schematic diagram of a multistage rectangular channel. (b) The trajectories of particles with diameter of 15 μm are shown. (c) Comparison of positions for particles with diameter of 15 μm (green), 10 μm (red) and 5 μm (cyan) at different locations between simulation results and experimental images[59] (the experimental images from ref. 59 are reprinted by permission from American Chemical Society).

rectangular channel, the top two focusing positions in the triangular channel, and top focusing position in the semicircular channel. Our simulation results agree well with the experimental ones (Fig. 10c).[58]

We further simulated the particle migration in a multistage rectangular channel.[59] As shown in Fig. 11a, the first-stage structure employs 5 loops of curved channel for particle separation, while the second-stage structure employs a 3D hydrodynamic focusing channel for single-position focusing. The multistage channel has a constant height of 130 μm throughout. In the first-stage, the radius of first loop is 1 cm and the spacing between two adjacent loops is 500 μm. The width of inlet1 and inlet2 is 425 μm and 75 μm, respectively. In the second-stage, there is a 90° curved structure with a radius of 250 μm. The width of inlet2, inlet3, and inlet4 is 100 μm, 200 μm, and 200 μm, respectively. The flow resistance matching structure employs a serpentine channel with a width of 400 μm and the radius of curvature is 250 μm. The flow rates are 0.17 m s^{-1} at the sheath inlet (inlet1) and 0.13 m s^{-1} at the sample inlet (inlet2), respectively. The sheath flow rate at the inlet3, inlet4, and inlet5 is 1.2 m s^{-1}, 0.4 m s^{-1}, and 0.4 m s^{-1}. In the first stage, the larger particles (10 μm and 15 μm) focus near the inner

wall whereas the small ones (5 μm) focus near the outer wall. Fig. 11b shows the trajectories of the particles with diameter of 15 μm. The migration of different particles in the curved structure is mainly determined by the competition between the inertial lift force and the Dean drag force. The Dean drag comes from the Dean vortex, which can be accurately obtained by the N–S equations. The Dean drag was taken into account through the first and second term on the right-hand side of eqn (12). Since the velocity profile in the main flow direction for the curved channel and the straight channel are consistent, the inertial lift in the corresponding straight channel was mapped on the cross-section of the curved channel by the third term of eqn (12). In the second stage, the particles focusing near the inner wall in the first stage are squeezed to a single focusing position. Particle positions predicted by simulations almost reproduce the experimental observations at different locations of (i), (ii), (iii), (iv), as shown in Fig. 11c.

IV. Conclusions

Recent developments in inertial microfluidics have proven its advantages for continuous focusing and separation of

microparticles. Based on the extensive direct numerical simulations of nearly 15 000 cases, we have constructed a database for distributions of inertial lift forces in three types of cross-section of straight microchannels in a wide parameter space. A machine learning assisted model was proposed to quickly obtain the inertial lift distributions for given channel shape, Reynolds number, and particle blockage ratio. The resultant inertial lift can be easily integrated into the Lagrangian tracking scheme to accurately predict the particle migration, as demonstrated by simulation and verification of two types of complex microchannels for practical applications. With the provided database and associated codes for the calculation of lift forces, we envision that researchers could expedite the development and optimization of inertial microfluidic devices for particle manipulations.

Author contributions

Conceptualization, J. S., X. C., G. H.; methodology, J. S., X. C., Y. Z., G. H.; software, J. S., X. C., Y. Z.; validation, J. S.; formal analysis, J. S., X. C.; investigation, J. S., X. C., G. H.; writing – original draft, J. S.; writing – review & editing, X. C., G. H.; funding acquisition, G. H.; supervision, G. H.

Conflicts of interest

There are no conflicts to declare.

Acknowledgements

References

1 G. Segre and A. Silberberg, *Nature*, 1961, **189**, 209.
2 H. A. Stone, A. D. Stroock and A. Ajdari, *Annu. Rev. Fluid Mech.*, 2004, **36**, 381–411.
3 D. Di Carlo, D. Irimia, R. G. Tompkins and M. Toner, *Proc. Natl. Acad. Sci. U. S. A.*, 2007, **104**, 18892–18897.
4 S. Shen, C. Ma, L. Zhao, Y. Wang, J.-C. Wang, J. Xu, T. Li, L. Pang and J. Wang, *Lab Chip*, 2014, **14**, 2525–2538.
5 J. Zhang, S. Yan, D. Yuan, G. Alici, N.-T. Nguyen, M. Ebrahimi Warkiani and W. Li, *Lab Chip*, 2016, **16**, 10–34.
6 H. Amini, W. Lee and D. Di Carlo, *Lab Chip*, 2014, **14**, 2739–2761.
7 P. Mukherjee, X. Wang, J. Zhou and I. Papautsky, *Lab Chip*, 2018, **19**, 147–157.
8 I. Lashgari, M. N. Ardekani, I. Banerjee, A. Russom and L. Brandt, *J. Fluid Mech.*, 2017, **819**, 540–561.
9 E. S. Asmolov, A. L. Dubov, T. V. Nizkaya, J. Harting and O. I. Vinogradova, *J. Fluid Mech.*, 2018, **840**, 613–630.
10 D. Stoecklein and D. Di Carlo, *Anal. Chem.*, 2019, **91**, 296–314.
11 Y. Morita, T. Itano and M. Sugihara-Seki, *J. Fluid Mech.*, 2017, **813**, 750–767.
12 B. P. Ho and L. G. Leal, *J. Fluid Mech.*, 1974, **65**, 365.
13 J. Su, X. Chen and G. Hu, *Phys. Fluids*, 2018, **30**, 032007.
14 C. Liu, G. Hu, X. Jiang and J. Sun, *Lab Chip*, 2015, **15**, 1168–1177.
15 X. Lu and X. Xuan, *Anal. Chem.*, 2015, **87**, 4560–4565.
16 C. Prohm and H. Stark, *Lab Chip*, 2014, **14**, 2115–2123.
17 K. Hood, S. Lee and M. Roper, *J. Fluid Mech.*, 2015, **765**, 452–479.
18 K. Hood, S. Kahkeshani, D. Di Carlo and M. Roper, *Lab Chip*, 2016, **16**, 2840–2850.
19 P. Vasseur and R. G. Cox, *J. Fluid Mech.*, 1976, **78**, 385.
20 J. A. Schonberg and E. J. Hinch, *J. Fluid Mech.*, 1989, **203**, 517.
21 E. S. Asmolov, *J. Fluid Mech.*, 1999, **381**, 63–87.
22 Q. Wang, D. Yuan and W. Li, *Micromachines*, 2017, **8**, 197.
23 D. R. Gossett, H. T. Tse, J. S. Dudani, K. Goda, T. A. Woods, S. W. Graves and D. Di Carlo, *Small*, 2012, **8**, 2757–2764.
24 J. Cruz, T. Graells, M. Wallden and K. Hjort, *Lab Chip*, 2019, **19**, 1257–1266.
25 S. Razavi Bazaz, A. Mashhadian, A. Ehsani, S. C. Saha, T. Krüger and M. Ebrahimi Warkiani, *Lab Chip*, 2020, **20**, 1023–1048.
26 X. M. Shao, Z. S. Yu and B. Sun, *Phys. Fluids*, 2008, **20**, 11.
27 B. Chun and A. J. C. Ladd, *Phys. Fluids*, 2006, **18**, 031704.
28 D. Di Carlo, J. F. Edd, K. J. Humphry, H. A. Stone and M. Toner, *Phys. Rev. Lett.*, 2009, **102**, 094503.
29 B. H. Yang, J. Wang, D. D. Joseph, H. H. Hu, T. W. Pan and R. Glowinski, *J. Fluid Mech.*, 2005, **540**, 109.
30 J. S. Park, S. H. Song and H. I. Jung, *Lab Chip*, 2009, **9**, 939–948.
31 Y. Zhang, J. Zhang, F. Tang, W. Li and X. Wang, *Anal. Chem.*, 2018, **90**, 1786–1794.
32 R. H. Pritchard, A. A. Zhukov, J. N. Fullerton, A. J. Want, F. Hussain, M. F. la Cour, M. E. Bashtanov, R. D. Gold, A. Hailes, E. Banham-Hall and S. S. Rogers, *Lab Chip*, 2019, **19**, 2456–2465.
33 A. Abdulla, W. Liu, A. Gholamipour-Shirazi, J. Sun and X. Ding, *Anal. Chem.*, 2018, **90**, 4397–4405.
34 N. Xiang, X. Shi, Y. Han, Z. Shi, F. Jiang and Z. Ni, *Anal. Chem.*, 2018, **90**, 9515–9522.
35 R. Khojah, R. Stoutamore and D. Di Carlo, *Lab Chip*, 2017, **17**, 2542–2549.
36 B. Harding, Y. M. Stokes and A. L. Bertozzi, *J. Fluid Mech.*, 2019, **875**, 1–43.
37 C. Liu, C. Xue, J. Sun and G. Hu, *Lab Chip*, 2016, **16**, 884–892.
38 Y. Zhou, L. Song, L. Yu and X. Xuan, *Microfluid. Nanofluid.*, 2017, **21**, 14.
39 R. Rasooli and B. Çetin, *Micromachines*, 2018, **9**, 433.
40 Q. M. Tan, *Dimensional analysis: with case studies in mechanics*, Springer-Verlag, Berlin Heidelberg, 2011.

41 D. L. Brown, W. D. Henshaw and D. J. Quinlan, *Overture: An object-oriented framework for solving partial differential equations*, 1997.

42 W. D. Henshaw and P. Fast, *Technical Report LA-UR-96-3468*, Los Alamos National Laboratory, 1998.

43 C. Robert, *CHANCE*, 2014, vol. 27, pp. 62–63.

44 M. I. Jordan and T. M. Mitchell, *Science*, 2015, **349**, 255–260.

45 J. R. Quinlan, *C4.5: programs for machine learning*, Morgan Kaufmann Publishers Inc., 1993.

46 V. Anagnostidis, B. Sherlock, J. Metz, P. Mair, F. Hollfelder and F. Gielen, *Lab Chip*, 2020, **20**, 889–900.

47 N. Wang, R. Liu, N. Asmare, C. H. Chu and A. F. Sarioglu, *Lab Chip*, 2019, **19**, 3292–3304.

48 D. E. Rumelhart, G. E. Hinton and R. J. Williams, *Nature*, 1986, **323**, 533–536.

49 N. Murata, S. Yoshizawa and S. Amari, *IEEE Trans. Neural Netw. Learn. Syst.*, 1994, **5**, 865–872.

50 J. Schmidhuber, *Neural Netw.*, 2015, **61**, 85–117.

51 M. T. Hagan and M. B. Menhaj, *IEEE Trans. Neural Netw. Learn. Syst.*, 1994, **5**, 989–993.

52 J. Sun, C. Liu, M. Li, J. Wang, Y. Xianyu, G. Hu and X. Jiang, *Biomicrofluidics*, 2013, **7**, 11802.

53 J. Sun, M. Li, C. Liu, Y. Zhang, D. Liu, W. Liu, G. Hu and X. Jiang, *Lab Chip*, 2012, **12**, 3952–3960.

54 N. Kolev, Drag, lift, and virtual mass forces, in *Multiphase Flow Dynamics 2*, Springer, Berlin, Heidelberg, 2011.

55 W. Tang, S. Zhu, D. Jiang, L. Zhu, J. Yang and N. Xiang, *Lab Chip*, 2020, **20**, 3485–3502.

56 N. Nakagawa, T. Yabu, R. Otomo, A. Kase, M. Makino, T. Itano and M. Sugihara-Seki, *J. Fluid Mech.*, 2015, **779**, 776–793.

57 A. Mashhadian and A. Shamloo, *Anal. Chim. Acta*, 2019, **1083**, 137–149.

58 J. Kim, J. Lee, C. Wu, S. Nam, D. Di Carlo and W. Lee, *Lab Chip*, 2016, **16**, 992–1001.

59 Q. Li, S. Cui, Y. Xu, Y. Wang, F. Jin, H. Si, L. Li and B. Tang, *Anal. Chem.*, 2019, **91**, 14133–14140.